Advances in Geo-Energy Research

Vol. 8, No. 2, p. 100-111, 2023

Original article

# A fractal effective permeability model for dual-wet porous media

Yue Shi[1,2]*, Yujia Guo[3], Hassan Dehghanpour[4], Haofeng Song[5]

[1]*School of Energy, China University of Geosciences, Beijing 100083, P. R. China*

[2]*Shaanxi Key Laboratory of Advanced Stimulation Technology for Oil & Gas Reservoirs, Xi'an Shiyou University, Xi'an 710065, P. R. China*

[3]*Deparment of Petroleum and Geosystems, The University of Texas at Austin, Austin, TX 78705, USA*

[4]*School of Mining and Petroleum Engineering, University of Alberta, Edmonton, AB T6G 2R3, Canada*

[5]*Production and Operation Management Department, China National Petroleum Corporation, Beijing 100018, P. R. China*

**Keywords:**
Effective permeability
dual-wettability
fractal theory
pore size distribution

**Cited as:**
Shi, Y., Guo, Y., Dehghanpour, H., Song, H. A fractal effective permeability model for dual-wet porous media. Advances in Geo-Energy Research, 2023, 8(2): 100-111.
https://doi.org/10.46690/ager.2023.05.04

**Abstract:**
Recent studies have shown that the pores of some unconventional rocks can be categorized into hydrophilic pores that boarded by inorganic minerals such as quartz and hydrophobic pores that within the organic matter. The rock which consists of both hydrophilic and hydrophobic pores shows a dual-wettability behavior. The previously-proposed imbibition transient analysis technique has been applied in characterizing the pore size distribution of the dual-wet rocks by analyzing comparative oil and water imbibition data. On the basis of the determined pore size distribution, a fractal model for estimating effective permeability of the dual-wet rock was proposed. The proposed model, together with the imbibition transient analysis technique, is able to estimate effective permeability of the dual-wet rocks by using imbibition data. The proposed model can also estimate the effective permeability of hydrophilic pores and hydrophobic pores. The proposed model takes injection pressure, wettability behavior and pore size distribution of the dual-wet rock into the consideration. Our sensitivity analyses show that injection pressure affects effective permeability and hydrophobic permeability by controlling the water saturation within hydrophobic pores. The rock with higher volumetric fraction of hydrophilic pores tends to have higher hydrophilic permeability and lower hydrophobic permeability. By keeping the porosity constant, effective permeability decreases as the volumetric fraction of small pores increases.

## 1. Introduction

Permeability has been commonly considered as one of the key inherent properties of the hydrocarbon-bearing sedimentary rocks. Permeability is the quantitative characterization of the reservoir's flow capacity (Peters, 2012a). Accurate determination of permeability is critical in reservoir evaluation, operation and management (Mahdaviara et al., 2020). However, accurately estimating permeability has never been a simple task due to the complex pore network of reservoir rocks, especially for unconventional rocks. Laboratory studies show that rock permeability can be affected by many parameters such as porosity, tortuosity, pore geometry and pore size distribution (PSD).

The widely accepted correlation for permeability and porosity is Carman-Kozeny equation (Kozeny, 1927; Carman, 1997). The Carman-Kozeny equation describes permeability in terms of porosity, tortuosity and surface area per grain volume. In Carman-Kozeny equation, the pore network is idealized as a pack of granular grains with uniform size. Dullien (1975) argued that a mean pore diameter cannot account for the variations in pore size of natural sedimentary rocks. Several mathematical models were developed by taking PSD into consideration (Millington and Quirk, 1961; Dullien, 1975).

Yandy Scientific Press

*Corresponding author.
*E-mail address*: yue_shi@cugb.edu.cn (Y. Shi); yguo@utexas.edu (Y. Guo); dehghanpour@ualberta.ca (H. Dehghanpour); haofeng.song@petrochina.com.cn (H. Song).



Received March 10, 2023; revised April 2, 2023; accepted April 20, 2023; available online April 25, 2023.

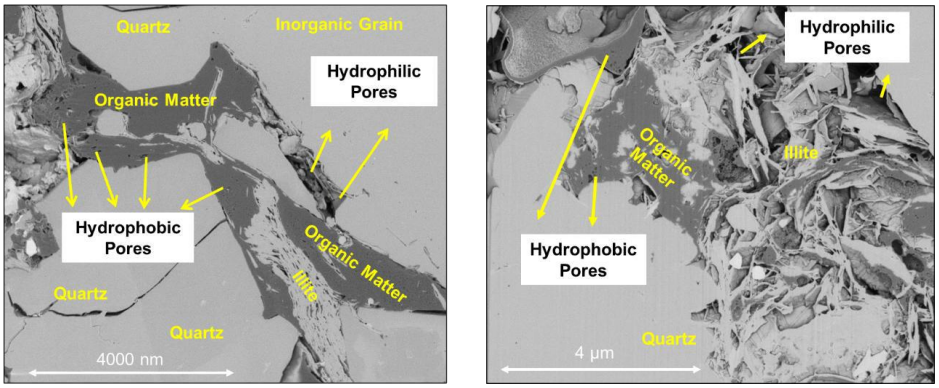


(a) (b)

**Fig. 1**. SEM images of one Montney sample from the dry-gas window (after Yassin et al. (2016)).

Millington and Quirk (1961) derived a permeability model by using PSD data which is obtained from mercury injection capillary pressure (MICP) test and water desorption isotherms. However, this permeability model fails to give satisfactory results in laminated sedimentary rocks. Dullien (1975) used MICP to determine PSD and developed a permeability model by idealizing the pore network as a bundle of straight tubes with wide and narrow segments. The model was validated by comparing estimated permeability with measured permeability of 14 conventional sandstones. Nuclear magnetic resonance (NMR), as a useful well-logging and core analysis technique, has also been used for determining PSD. Several scholars (Hidajat et al., 2002; Rezaee et al., 2012) incorporated the NMR-determined PSD into their permeability models.

Fractal theory was firstly introduced by Mandelbrot (1967) and has been successfully applied in describing the complex pore network of natural sedimentary rocks (Perfect and Kay, 1995; Tan et al., 2015; Xia et al., 2019). For the rock with fractal geometry, the number of pores with a particular size can be expressed as a function of pore diameter and fractal dimension ($D$) (Mandelbrot, 1967). Several researchers have applied the fractal theory to estimate permeability (Yu et al., 2002; Xu and Yu, 2008; Li et al., 2018). Yu et al. (2002) developed a fractal permeability model for the bi-dispersed porous media, which consists of macro-pores between the grains and micro-pores within the grains. Permeability was estimated by five controlling parameters including $D$ and maximum pore diameter. Xu and Yu (2008) proposed a more generalized model by reducing the number of controlling parameter in the previous model (Yu et al., 2002). Zheng and Yu (2012) presented a fractal model for predicting permeability in the dual porosity porous media which consists of matrix and fracture.

Fractal permeability models have also been developed for unconventional rocks. Geng et al. (2016) presented a model for natural gas flow in shales. The sensitivity analysis revealed that validity of the permeability model for shale rocks is questionable when total organic carbon (TOC) content can not be ignored. Chen and Yao (2017) argued that the low-permeability tight rocks tend to have high irreducible water saturation due to abundance of small pores. A fractal permeability model was developed by coupling irreducible water saturation for tight rocks. Many other fractal permeability models have also been developed aiming to effectively estimate permeability for unconventional rocks (Cai et al., 2014; Wang et al., 2015; Wang et al., 2017). However, the wettability behavior of unconventional rocks is not included in most existing fractal permeability models.

The wettability behavior of unconventional rocks such as shale and tight sandstone has been extensively studied (Gao et al., 2018). Odusina et al. (2011) studied wettability of shale samples from Barnett, Floyd and Woodford Formations by using the NMR technique. The strong oil-wet behavior of theses samples is contributed to the pores within the organic matter. Lan et al. (2015) performed comparative oil and water imbibition test on the rocks from the Montney tight-gas Formation. The strong oil-wet behavior is also concluded to be related to the abundance of organic matter. Yassin et al. (2016) reviewed results of imbibition data, scanning electron microscope (SEM)/energy-dispersive X-ray spectroscopy analyses, MICP tests and organic petrography and proposed the concept of dual-wet behavior. The pore network of the dual-wet rocks can be generally divided into two parts: the pores surrounded by inorganic minerals such as quartz, feldspar and calcite are hydrophilic while the pores primarily within the organic matter are hydrophobic, as evidenced in Fig. 1. Yassin et al. (2017) also detected the dual-wettability behavior in the Duvernay shale samples by conducting imbibition tests and analyzing SEM/EDS images. Zhang et al. (2018) developed a permeability model to describe the water transport in shale with dual-wet behavior. The model was developed based on a constructed 2-dimensional sample by analyzing SEM images. In this study, we propose a new fractal permeability model for dual-wet rocks by using the comparative oil and water imbibition data.

The basic theory and assumptions of the proposed fractal permeability model is introduced in Section 2. Section 3 presents the detailed derivation of the proposed model and

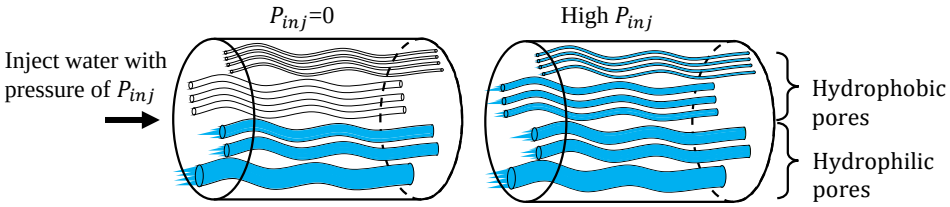


**Fig. 2**. Schematic view of water flow through an idealized dual-wet rock.

Section 4 describes how the unknown parameters in the proposed model are determined. In Section 5, we apply the proposed model to estimate the permeability of 13 pairs of rocks with dual-wettability behavior. Sensitivity analysis is performed to investigate the effect of injection pressure ($P_{inj}$), wettability behavior and hydrophobic pore size distribution on permeability in Section 6. Section 7 and Section 8 discuss the limitations and main conclusions of this work.

## 2. Theory and assumptions

In this paper, the effective permeability ($K_e$) of water in the rock with both hydrophilic and hydrophobic pores is modeled. As discussed in previous studies (Lan et al., 2015; Yassin et al., 2016; Shi et al., 2019), the pore network of some unconventional rocks is considered as a dual-wet system, which consists of both hydrophilic and hydrophobic pores. As shown in Fig. 2, the pore network of the rock is represented by a bundle of tortuous elongated pores without any interconnection. All the pores are exposed to the water at the left end of the rock, and are continuously extended to the right end of the rock. This simplified pore network has been widely used in previous studies for modeling fluid flow in porous media and characterizing petrophysical properties of sedimentary rocks (Dullien, 2012; Zhang et al., 2019). The rock is initially saturated with air ($S_{wi}$ = 0) and then water is injected from one face of the rock with injection pressure of $P_{inj}$. Fig. 2 shows that water flow can only occur in hydrophilic pores when $P_{inj}$ is zero. This is because water can spontaneously flow through hydrophilic pores driven by capillary pressure. However, water cannot flow through hydrophobic pores since the capillary pressure of the pores are negative. When $P_{inj}$ is high enough to overcome the entry capillary pressure of hydrophobic pores, water drain the air in the hydrophobic pores. Once water flow is stabilized at a certain $P_{inj}$, $K_e$ can be calculated. In this paper, we will derive a fractal effective permeability model for water in the idealized dual-wet rock.

## 3. Model derivation

The laminar flow rate of a Newtonian fluid through a tortuous pore is modified from the Hagen-Poiseuille's equation:

$$q(\lambda) = \frac{\pi\lambda^4}{128\mu}\frac{\Delta P}{\tau L_s} \tag{1}$$

where $q$ is flow rate of fluid in a single pore; $\lambda$ is the pore diameter and $\mu$ is the liquid viscosity; $L_s$ is straight length of the liquid inside a pore, which can also be considered as the length of the rock; $\Delta P$ is the driving force for fluid flow through the pore. The tortuosity ($\tau$) of a single pore is defined as the ratio of the tortuous length of liquid inside the pore ($L_f$) over $L_s$ (Bear, 2013):

$$\tau = \frac{L_f}{L_s} \tag{2}$$

Based on fractal theory (Mandelbrot, 1967), the number of pores with a particular diameter is a function of $\lambda$ and $D$. $D$ has the range of 0 to 2 in the two-dimensional space. The incremental number of pores ($n(\lambda)$) with diameters in the range of $\lambda$ to $\lambda+$ d$\lambda$ can be obtained by (Cai et al., 2012):

$$n(\lambda) = -\mathrm{d}N_f = \frac{4A_f}{\pi\lambda_{\max}^{2-D}}\frac{(2-D)\phi'}{1-\left(\frac{\lambda_{\min}}{\lambda_{\max}}\right)^{2-D}}\lambda^{-(D+1)}\mathrm{d}\lambda \tag{3}$$

where $A_f$ is cross-sectional area of rock. $\phi'$ is named as "surface porosity", which is the ratio of cross-sectional area of pores to $A_f$ (Shi et al., 2018). $\lambda_{\max}$ and $\lambda_{\min}$ are maximum and minimum diameters of pores in the rock. The flow rate in the pores with diameter of $\lambda$ ($Q(\lambda)$) can be obtained by multiplying Eqs. (1) and (3):

$$Q(\lambda) = \frac{\Delta P A_f(2-D)\phi'}{32\mu\tau L_s(\lambda_{\max}^{2-D}-\lambda_{\min}^{2-D})}\lambda^{3-D}\mathrm{d}\lambda \tag{4}$$

For the dual-wet rocks, the flow rate through hydrophilic pores ($Q_{hl}$) can be calculated by:

$$\begin{aligned} Q_{hl} &= \int_{\lambda_{\min\_hl}}^{\lambda_{\max\_hl}} Q(\lambda)\mathrm{d}\lambda \\ &= \frac{\Delta P A_f \phi_{hl}'(2-D_{hl})}{32\mu\tau_{hl}L_s(4-D_{hl})}\frac{\lambda_{\max\_hl}^{4-D_{hl}}-\lambda_{\min\_hl}^{4-D_{hl}}}{\lambda_{\max\_hl}^{2-D_{hl}}-\lambda_{\min\_hl}^{2-D_{hl}}} \end{aligned} \tag{5}$$

where $\lambda_{\max\_hl}$ and $\lambda_{\min\_hl}$ are maximum and minimum pore diameters of hydrophilic pores, respectively; $D_{hl}$ and $\tau_{hl}$ are fractal dimension and average tortuosity of hydrophilic pores, respectively; $\phi_{hl}'$ is the ratio of cross-sectional area of hydrophilic pores ($A_{hl}$) to $A_f$. Similarly, the flow rate through hydrophobic pores ($Q_{hb}$) can also be obtained by:

$$\begin{aligned} Q_{hb} &= \int_{\lambda_{\min\_hb}}^{\lambda_{\max\_hb}} Q(\lambda)\mathrm{d}\lambda \\ &= \frac{\Delta P A_f \phi_{hb}'(2-D_{hb})}{32\mu\tau_{hb}L_s(4-D_{hb})}\frac{\lambda_{\max\_hb}^{4-D_{hb}}-\lambda_{\mathrm{minc}\_hb}^{4-D_{hb}}}{\lambda_{\max\_hb}^{2-D_{hb}}-\lambda_{\min\_hb}^{2-D_{hb}}} \end{aligned} \tag{6}$$

where $\lambda_{\max\_hb}$ and $\lambda_{\min\_hb}$ are the maximum and minimum pore diameters of hydrophobic pores, respectively; $D_{hb}$ and $\tau_{hb}$ are fractal dimension and average tortuosity of hydrophobic pores, respectively; $\phi_{hb}'$ is the ratio of cross-sectional area of hydrophobic pores ($A_{hb}$) to $A_f$. It should be noted that

in Eq. (6), we use $\lambda_{minc\_hb}$ instead of $\lambda_{min\_hb}$ as the lower limit of integration. We define $\lambda_{minc\_hb}$ as the minimum diameter of hydrophobic pores that are open to water flow. Since water cannot flow through hydrophobic pores unless $P_{inj}$ exceeds entry capillary pressure, $\lambda_{minc\_hb}$ is a pressure-dependent variable and can be calculated can be calculated by:

$$\lambda_{minc\_hb} = \frac{4\sigma|\cos\theta_{hb}|}{P_{inj}} \tag{7}$$

where $\sigma$ is surface tension of water and $\theta_{hb}$ is air-liquid contact angle of water in hydrophobic pores. Since $\theta_{hb}$ is larger than 90°, absolute bracket is used in Eq. (7) to make the term positive. Based on Darcy's law, the effective permeability of water in hydrophilic pores ($K_{hl}$) can be obtained by:

$$K_{hl} = \frac{\mu L_s Q_{hl}}{\Delta P A_f} = \frac{\phi_{hl}'(2-D_{hl})}{32\tau_{hl}(4-D_{hl})} \frac{\lambda_{max\_hl}^{4-D_{hl}} - \lambda_{min\_hl}^{4-D_{hl}}}{\lambda_{max\_hl}^{2-D_{hl}} - \lambda_{min\_hl}^{2-D_{hl}}} \tag{8}$$

Similarly, the effective permeability of water in hydrophobic pores ($K_{hb}$) can be obtained by:

$$K_{hb} = \frac{\mu L_s Q_{hb}}{\Delta P A_f} = \frac{\phi_{hb}'(2-D_{hb})}{32\tau_{hb}(4-D_{hb})} \frac{\lambda_{max\_hb}^{4-D_{hb}} - \lambda_{minc\_hb}^{4-D_{hb}}}{\lambda_{max\_hb}^{2-D_{hb}} - \lambda_{min\_hb}^{2-D_{hb}}} \tag{9}$$

Inserting Eq. (7) into Eq. (9) gives:

$$K_{hb} = \frac{\phi_{hb}'(2-D_{hb})}{32\tau_{hb}(4-D_{hb})} \frac{\lambda_{max\_hb}^{4-D_{hb}} - (4\sigma|\cos\theta_{hb}|/P_{inj})^{4-D_{hb}}}{\lambda_{max\_hb}^{2-D_{hb}} - \lambda_{min\_hb}^{2-D_{hb}}} \tag{10}$$

Eqs. (8) and (10) are final equations of $K_{hl}$ and $K_{hb}$ for the dual-wet rock, respectively. The total flow rate through both hydrophilic and hydrophobic pores of the dual-wet rock ($Q_T$) can be obtained by:

$$Q_T = Q_{hl} + Q_{hb} \tag{11}$$

Thus, we can get the effective permeability of the dual-wet rock ($K_e$) by:

$$\begin{aligned} K_e &= \frac{\mu L_s Q_T}{\Delta P A_f} = \frac{\mu L_s (Q_{hl+Q_{hb}})}{\Delta P A_f} = K_{hl} + K_{hb} \\ &= \frac{\phi_{hl}'(2-D_{hl})}{32\tau_{hl}(4-D_{hl})} \frac{\lambda_{max\_hl}^{4-D_{hl}} - \lambda_{minc\_hl}^{4-D_{hl}}}{\lambda_{max\_hl}^{2-D_{hl}} - \lambda_{min\_hl}^{2-D_{hl}}} \\ &+ \frac{\phi_{hb}'(2-D_{hb})}{32\tau_{hb}(4-D_{hb})} \frac{\lambda_{max\_hb}^{4-D_{hb}} - (4\delta|\cos\theta_{hb}|/P_{inj})^{4-D_{hb}}}{\lambda_{max\_hb}^{2-D_{hb}} - \lambda_{min\_hb}^{2-D_{hb}}} \end{aligned} \tag{12}$$

Eq. (12) is the final equation for effective permeability of water in the dual-wet rock. As shown in Eqs. (10) and (12), $K_{hb}$ and $K_e$ are $P_{inj}$-dependent variables. As water can only flow through hydrophobic pores when $P_{inj}$ exceeds entry capillary pressure, higher $P_{inj}$ results in water flow through more hydrophobic pores, which leads to higher water saturation ($S_w$) in the rock. Therefore, the value of $P_{inj}$ changes $K_e$ and $K_{hb}$ by affecting $S_w$. For $K_{hl}$, since water is wetting phase in all the hydrophilic pores, water can spontaneously flow through them regardless of $P_{inj}$, leading to a constant value of $K_{hl}$. The effect of $P_{inj}$ on $K_e$, $K_{hl}$ and $K_{hb}$ of the dual-wet rock will be discussed in detail in Section 6.

## 4. Parameters determination

In this section, we present the methods for determining unknown parameters in Eq. (12). $\lambda_{max\_hl}$ and $\lambda_{max\_hb}$ are estimated by using the available MICP data. In the MICP test, the pressure corresponding to the start of mercury intrusion is converted to $\lambda_{maxMICP}$ using the Young-Laplace equation. As presented in our previous study (Shi et al., 2019), we assume $\lambda_{max\_hl} = \lambda_{max\_hb} = \lambda_{maxMICP}$. $\lambda_{min\_hl}$ and $\lambda_{min\_hb}$ can also be estimated by the MICP test. However, for some of the tight rocks, even a maximum mercury pressure of 400 MPa is not sufficient to detect $\lambda_{min}$ (Lan et al., 2015). In our previous studies (Shi et al., 2018, 2019), we proposed an alternative way to estimate $\lambda_{min}$ by analyzing the equilibrium time of imbibition profile ($t_{eq}$):

$$\lambda_{min} = \frac{4\mu(L_s\tau)^2}{\sigma\cos\theta t_{eq}} \tag{13}$$

where $\theta$ is contact angle. By analyzing the imbibition data of Duvernay shale and Montney tight rocks, previous works (Lan et al., 2015; Yassin et al., 2016) presented that water can spontaneously imbibe into hydrophilic pores and oil can spontaneously imbibe into both hydrophobic and hydrophilic pores. Therefore, Eq. (13) can be used to estimate $\lambda_{min\_hl}$ by water imbibition data and $\lambda_{min\_hb}$ by oil imbibition data (Shi et al., 2019).

Based on the previous studies (Shi et al., 2018, 2019), $\phi_{hl}'$ and $\phi_{hb}'$ can be modelled by:

$$\phi_{hl}' = \frac{\phi_{hl}}{\tau_{hl}} \tag{14}$$

$$\phi_{hb}' = \frac{\phi_{hb}}{\tau_{hb}} \tag{15}$$

where $\tau_{hl}$ and $\tau_{hb}$ are average tortuosity of hydrophilic and hydrophobic pores, respectively. $\phi_{hl}$ is the ratio of hydrophilic pore volume ($V_{hl}$) to bulk volume ($V_B$) and $\phi_{hb}$ is the ratio of hydrophobic pore volume ($V_{hb}$) to $V_B$. In the previous study (Shi et al., 2019), we obtained total pore volume ($V_{hl+hb}$) and $V_{hl}$ from oil and water imbibition tests, respectively.$V_{hl+hb}$ is obtained from equilibrated imbibed volume of oil and $V_{hl}$ is obtained from equilibrated imbibed volume of water. $V_{hb}$ is estimated by subtracting $V_{hl}$ from $V_{hl+hb}$. Thus, once $\tau_{hl}$ and $\tau_{hb}$ are determined, $\phi_{hl}'$ and $\phi_{hb}'$ can be calculated accordingly.

Our previous work (Shi et al., 2019) proposed an imbibition transient analysis method to determine $\tau$ and $D$ by fitting the proposed spontaneous imbibition model with experimental data. $D_{hl+hb}$ and $\tau_{hl+hb}$ are obtained by fitting oil imbibition data and $D_{hl}$ and $\tau_{hl}$ are obtained by fitting water imbibition data. Here, we present how $D_{hb}$ and $\tau_{hb}$ can be determined.

Previous fractal studies (Wu and Yu, 2007; Yu et al., 2009) show that the total number of pores in the rock ($N_f$) can be calculated by:

$$N_f = \frac{4A_f}{\pi\lambda_{max}^{2-D}} \frac{2-D}{D} \frac{\phi'}{1-\left(\frac{\lambda_{min}}{\lambda_{max}}\right)^{2-D}} \lambda_{min}^{2-D} \tag{16}$$

For the dual-wet rock, the total number of hydrophilic pores ($N_{fhl}$), hydrophilic pores ($N_{fhb}$) and all pores ($N_{fhl+hb}$) follow Eqs. (17) to (19), respectively:

$$N_{fhl} = \frac{4A_f}{\pi\lambda_{\text{maxMICP}}^{2-D_{hl}}} \frac{2-D_{hl}}{D_{hl}} \frac{\phi'_{hl}}{1-\left(\frac{\lambda_{\min\_hl}}{\lambda_{\text{maxMICP}}}\right)^{2-D_{hl}}} \lambda_{\min\_hl}^{2-D_{hl}} \quad (17)$$

$$N_{fhb} = \frac{4A_f}{\pi\lambda_{\text{maxMICP}}^{2-D_{hb}}} \frac{2-D_{hb}}{D_{hb}} \frac{\phi'_{hb}}{1-\left(\frac{\lambda_{\min\_hb}}{\lambda_{\text{maxMICP}}}\right)^{2-D_{hb}}} \lambda_{\min\_hb}^{2-D_{hb}} \quad (18)$$

$$N_{fhl+hb} = \frac{4A_f}{\pi\lambda_{\text{maxMICP}}^{2-D_{hl+hb}}} \frac{2-D_{hl+hb}}{D_{hl+hb}} \cdot \frac{\phi'_{hl}+\phi'_{hb}}{1-\left(\frac{\lambda_{\min\_hl+hb}}{\lambda_{\text{maxMICP}}}\right)^{2-D_{hl+hb}}} \lambda_{\min}^{2-D_{hl+hb}} \quad (19)$$

where $\lambda_{\min\_hb}$ is used in Eq. (19) because hydrophobic pores are primarily nanopores that are within organic matter and are generally smaller than hydrophilic pores (Odusina et al., 2011; Yassin et al., 2016; Yassin et al., 2020). $N_{fhl}$, $N_{fhb}$ and $N_{fhl+hb}$ are related by:

$$N_{fhl+hb} = N_{fhl} + N_{fhb} \quad (20)$$

Since $\tau$ is average tortuosity of pores, $\tau_{hl+hb}$ can be calculated by:

$$\tau_{hl+hb} = \frac{N_{fhl}\cdot\tau_{hl} + N_{fhb}\cdot\tau_{hb}}{N_{fhl+hb}} \quad (21)$$

By inserting Eqs. (17) to (19) into Eqs. (20) and (21), $D_{hb}$ and $\tau_{hb}$ can be obtained by solving Eqs. (20) and (21) simultaneously.

In summary, $\lambda_{\max\_hl}$ and $\lambda_{\max\_hb}$ are estimated from available MICP data; $\lambda_{\min\_hl}$ and $\lambda_{\min\_hb}$ are calculated by Eq. (13) through analyzing equilibrium time of imbibition data; $\phi_{hl}$ and $\phi_{hb}$ are obtained from equilibrated imbibed volume of water and oil; $\phi_{hl}'$and $\phi_{hb}'$ are calculated by Eqs. (14) and (15), respectively; $D_{hl}$ and $\tau_{hl}$ are obtained by fitting water imbibition data and $D_{hb}$ and $\tau_{hb}$ are calculated by solving Eqs. (20) and (21) simultaneously. Once the unknown parameters in Eq. (12) are determined by analyzing MICP and imbibition data, $K_{hl}$, $K_{hb}$ and $K_e$ can be obtained. The detailed procedure of determining parameters have been discussed in our previous work (Shi et al., 2019).

## 5. Model application

In this section, we calculate $K_{hl}$, $K_{hb}$ and $K_e$ of 13 pairs of twin rocks from the Montney Formation (Lan et al., 2015). The Montney Formation covers a large geographic area of approximately 130,000 km$^2$ with the thickness of 100 to 300 m in Alberta and British Columbia, Canada (Nieto et al., 2009). The Montney Formation generally comprises fine siltstones with minor shales (Davies, 1997). Among the selected rocks, 5 pairs are from the Upper Montney (UMT) Formation, 4 pairs are from Lower Montney (LMT) Formation and 4 pairs from Gordondale area of the Montney (GMT) Formation. The properties of the rocks including depth, $A_f$, $L_s$, effective porosity ($\phi$), air permeability ($K_{air}$) are listed in Table 1 (Lan et al., 2015). $\phi$ is estimated by helium porosimetry and $K_{air}$ is measured by using pulse-decay method. Table 1 also lists TOC content of the rocks measured by using Rock-Eval 6 technique.

The determined values of parameters in Eq. (12) are presented in Appendix A. $\sigma$ = 72.7 mN/m is used as surface tension of water. $\theta_{hb}$ is contact angle of air/water at pore scale, which is affected by surface properties of hydrophobic pores. For the selected Montney rocks, hydrophobic pores are within or coated by organic matter. Jagadisan and Heidari (2019) presented that air/water contact angle changes from 40° on low thermally mature kerogen to 125° on high thermally mature kerogen. Here, we use $\theta_{hb}$ = 125° in Eq. (12) because the majority of Montney Formation has high level of thermal maturity and lies within gas generating window (Egbobawaye, 2017). Based on the selected values of $\sigma$ and $\theta_{hb}$, water can intrude into the hydrophobic pore with diameter of 1 nm under $P_{inj}$ of 167 MPa. In this section, we set $P_{inj}$ to be 200 MPa. Under this high $P_{inj}$ , all the pores can be flooded through for the selected rocks.

Table 2 lists calculated values of $K_{hl}$, $K_{hb}$ and $K_e$ for the selected rocks. $K_{hl}$ and $K_{hb}$ are obtained by Eq. (8) and (10), respectively. $K_e$ is the summation of $K_{hl}$ and $K_{hb}$, which can also be obtained by Eq. (12). Generally,$K_e$ of UMT and GMT rocks is in order of $10^{-4}$ to $10^{-3}$ mD and $K_e$ of LMT rocks is in order of $10^{-5}$ to $10^{-4}$ mD. The lower $K_e$ of LMT rocks compared with that of UMT and GMT rocks indicates that LMT rocks have more compacted pore space, which is consistent with the fact that porosity of LMT rocks is in general lower than that of UMT and GMT rocks (Table 1).

Fig. 3(a) compares calculated values of $K_e$ with $K_{air}$ listed in Table 1. For all the selected rocks, the values of $K_e$ obtained by Eq. (12) are smaller than those of $K_{air}$ measured by pulse decay technique. In Eq. (12), we obtain $\phi_{hl+hb}$ from equilibrated imbibed volume of oil in the imbibition test. As presented in our previous work (Shi et al., 2019), oil can generally imbibe into 70%-90% of effective pore volume. Thus, 10% to 30% of effective PV is not accessible for oil and $\phi_{hl+hb} < \phi$. The underestimation of $\phi_{hl+hb}$ could be one of the explanations for lower values of $K_e$ compared with that of $K_{air}$. Another explanation is that $\lambda_{\max\_hl}$ and $\lambda_{\max\_hb}$ might be underestimated in Eq. (12). As discussed in Section 4, $\lambda_{\max\_hl}$ and $\lambda_{\max\_hb}$ are assumed to be equal to $\lambda_{\max MICP}$, which is obtained from available MICP data. In the MICP test, the intrusion of mercury is considered to be a drainage process that is mainly controlled by the pore-throat size distribution of rocks (Wardlaw and Taylor, 1976). Therefore, the values of $\lambda_{\max\_hb}$ and $\lambda_{\max\_hb}$ in Eq. (12) correspond to the maximum pore-throat diameter. As larger values of $\lambda_{\max\_hl}$ and $\lambda_{\max\_hb}$ give higher $K_e$, the use of MICP data may lead to underestimation of $K_e$. The aspect ratio (AR) has a wide range from has a wide range from 1.2 to several hundreds (Wardlaw and Yu, 1988; Jerauld and Salter, 1990). Here, we assume AR to be 2 and 3 and consider $\lambda_{\max\_hl}$ and $\lambda_{\max\_hb}$ in Eq. (12) as the maximum pore-body diameter. In other words, values of 2 × $\lambda_{\text{maxMICP}}$ and 3 × $\lambda_{\text{maxMICP}}$ are used in Eq. (12) when AR = 2 and AR = 3, respectively. All the other parameters in Eq. (12) remains the same. Fig. 3(b) shows $K_e$ calculated by Eq. (12) with assuming different values of AR. The data with AR = 1 is the original data as plotted in Fig. 3(a). With increasing AR, $K_e$ increases for all the rocks. When AR = 3, $K_e$ of UMT and GMT rocks shows

**Table 1**. Dimensions and petrophysical properties for UMT, GMT and LMT rocks.

| Rock | Depth (m) | $A_f$ (cm$^2$) | $L_s$ (cm) | $\phi$ (fraction) | $K_{air}$ (mD) | TOC (wt%) |
|---|---|---|---|---|---|---|
| UMT1$_o$ | 2127.21 | 10.75 | 6.60 | 0.051 | - | 0.83 |
| UMT1$_w$ | 2127.55 | 10.75 | 6.60 | 0.047 | - | 1.09 |
| UMT2$_o$ | 2130.20 | 10.75 | 6.80 | 0.057 | $3.89\times10^{-3}$ | 0.89 |
| UMT2$_w$ | 2130.57 | 10.75 | 6.90 | 0.049 | $3.89\times10^{-3}$ | 0.83 |
| UMT3$_o$ | 2137.45 | 10.75 | 6.60 | 0.064 | $2.35\times10^{-2}$ | 1.30 |
| UMT3$_w$ | 2137.83 | 10.75 | 6.70 | 0.069 | $2.35\times10^{-2}$ | 1.04 |
| UMT4$_o$ | 2144.01 | 10.75 | 6.70 | 0.072 | $1.05\times10^{-1}$ | 0.98 |
| UMT4$_w$ | 2144.37 | 10.75 | 6.95 | 0.078 | $1.05\times10^{-1}$ | 0.87 |
| UMT5$_o$ | 2150.74 | 10.75 | 6.75 | 0.057 | $4.42\times10^{-3}$ | 0.21 |
| UMT5$_w$ | 2151.17 | 10.75 | 6.50 | 0.051 | $4.42\times10^{-3}$ | 0.38 |
| GMT1$_o$ | 2274.70 | 11.21 | 5.54 | 0.052 | $9.02\times10^{-3}$ | 1.13 |
| GMT1$_w$ | 2274.66 | 11.17 | 5.86 | 0.052 | $9.02\times10^{-3}$ | 1.13 |
| GMT2$_o$ | 2285.12 | 11.25 | 5.97 | 0.044 | $5.25\times10^{-3}$ | 1.14 |
| GMT2$_w$ | 2285.16 | 11.31 | 5.99 | 0.044 | $5.25\times10^{-3}$ | 1.14 |
| GMT3$_o$ | 2188.13 | 11.26 | 6.62 | 0.061 | $4.00\times10^{-2}$ | 1.32 |
| GMT3$_w$ | 2188.18 | 11.25 | 6.12 | 0.061 | $4.00\times10^{-2}$ | 1.32 |
| GMT4$_o$ | 2200.76 | 11.28 | 6.52 | 0.067 | $4.00\times10^{-2}$ | 1.08 |
| GMT4$_w$ | 2200.80 | 11.27 | 6.37 | 0.067 | $4.00\times10^{-2}$ | 1.08 |
| LMT1$_o$ | 2323.20 | 10.75 | 6.75 | 0.043 | $1.50\times10^{-2}$ | 1.57 |
| LMT1$_w$ | 2323.53 | 10.75 | 6.70 | 0.040 | $1.50\times10^{-2}$ | 1.82 |
| LMT2$_o$ | 2329.80 | 10.75 | 6.90 | 0.029 | $2.33\times10^{-3}$ | 1.75 |
| LMT2$_w$ | 2330.22 | 10.75 | 6.95 | 0.032 | $2.33\times10^{-3}$ | 1.85 |
| LMT3$_o$ | 2340.29 | 10.75 | 6.55 | 0.036 | $2.04\times10^{-3}$ | 1.89 |
| LMT3$_w$ | 2340.61 | 10.75 | 6.60 | 0.040 | $2.04\times10^{-3}$ | 1.72 |
| LMT4$_o$ | 2346.98 | 10.75 | 6.75 | 0.041 | $1.01\times10^{-2}$ | 1.32 |
| LMT4$_w$ | 2347.28 | 10.75 | 6.60 | 0.045 | $1.01\times10^{-2}$ | 1.55 |

Note: Subscripts $o$ and $w$ represent oil and water, respectively.

a good match with $K_{air}$. For LMT rocks, the values of $K_e$ are still lower than that of $K_{air}$, which indicates LMT rocks might have a relatively larger aspect ratio than UMT and GMT rocks. Therefore, a reasonably fair match between $K_e$ and $K_{air}$ can be achieved if proper values of $\lambda_{\max\_hl}$ and $\lambda_{\max\_hb}$ are used in Eq. (12). It is worth noting that the mismatch between $K_e$ and $K_{air}$ could also be due to that fact that some pores were not accessed in imbibition.

Fig. 4(a) plots $K_{hb}$ versus TOC content as listed in Table 1. A negative correlation between $K_{hb}$ and TOC can be observed, although the data are quite scattered. A previous study (Lan et al., 2015) presented that higher TOC indicates higher amount of organic matter, which in turn, results in higher fraction of hydrophobic pores ($\phi_{hb}/\phi_{hl+hb}$). Therefore, we expect to see higher $K_{hb}$ for the rock with higher TOC. However, as shown in Table 1, LMT rocks generally have lower permeability and porosity but higher TOC than UMT rocks. Thus, the negative correlation between $K_{hb}$ and TOC can be explained by the fact that the rocks with higher TOC content tends to have more compacted pore space. To prove this explanation, we normalize $K_{hb}$ by $K_e$ and plot the value of $K_{hb}/K_e$ versus TOC, as shown in Fig. 6b. The positive correlation between $K_{hb}/K_e$ and TOC indicates that the rock with higher TOC tends to have higher fraction of hydrophobic pores, which results in higher $K_{hb}/K_e$. This is in agreement with the results of SEM, showing that hydrophobic pores are mainly within or coated by organic matters (Lan et al., 2015; Yassin et al., 2016).

## 6. Sensitivity analysis

In this section, we firstly perform sensitivity analysis to investigate the effect of $P_{inj}$ on $K_e$, $K_{hl}$ and $K_{hb}$ for the selected dual-wet rocks. Then, we quantitatively evaluate rock wettability by using $\theta_{hb}$ and defining a Modified Wettability

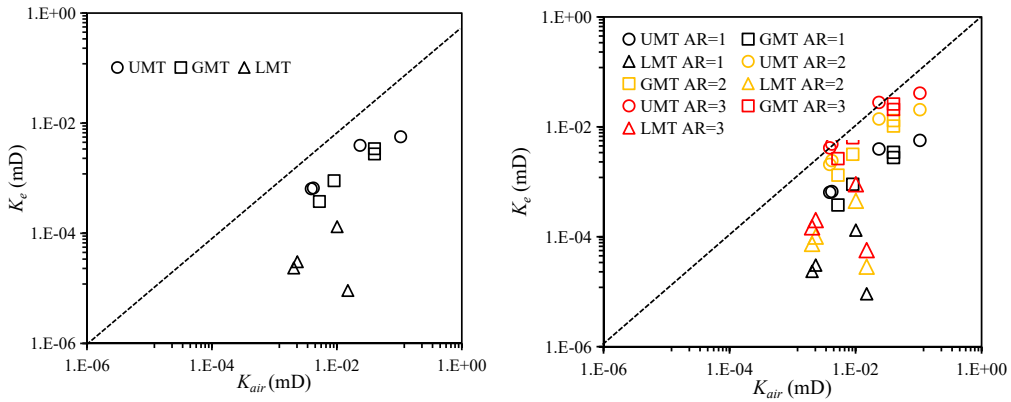


**Fig. 3**. Comparison of $K_{air}$ vs. (a) $K_e$ and (b) $K_e$ with assuming maximum pore-body diameter and different values of AR.

**Table 2**. Calculated values of permeabilities for the selected rocks.

| Rock | $K_e$ (mD) | $K_{hl}$ (mD) | $K_{hb}$ (mD) |
|---|---|---|---|
| UMT1 | 1.14E-03 | 6.17E-04 | 5.23E-04 |
| UMT2 | 6.44E-04 | 3.56E-04 | 2.88E-04 |
| UMT3 | 3.96E-03 | 1.74E-03 | 2.21E-03 |
| UMT4 | 5.67E-03 | 3.23E-03 | 2.44E-03 |
| UMT5 | 6.65E-04 | 4.25E-04 | 2.40E-04 |
| GMT1 | 9.03E-04 | 3.54E-04 | 5.48E-04 |
| GMT2 | 3.79E-04 | 2.08E-04 | 1.71E-04 |
| GMT3 | 3.44E-03 | 1.06E-03 | 2.39E-03 |
| GMT4 | 2.76E-03 | 1.08E-03 | 1.69E-03 |
| LMT1 | 9.15E-06 | 1.75E-06 | 7.40E-06 |
| LMT2 | 3.05E-05 | 9.22E-06 | 2.12E-05 |
| LMT3 | 2.34E-05 | 6.72E-06 | 1.67E-05 |
| LMT4 | 1.32E-04 | 1.96E-05 | 1.12E-04 |

Index (MWI) based on imbibition data. $\theta_{hb}$ and MWI are used to examine the effect of rock wettability on $K_e$, $K_{hl}$ and $K_{hb}$. We also investigate the effect of hydrophobic pore size distribution (PSD$_{hl}$) on $K_e$ by changing $D_{hb}$ and the ratio of $\lambda_{\max\_hb}/\lambda_{\min\_hb}$.

## 6.1 Effect of $P_{inj}$

As discussed before, $K_{hb}$ and $K_e$ are $P_{inj}$-dependent variables. In Section 5, we set $P_{inj}$ to be 200 MPa to ensure $S_w$ = 100%. Here, we calculate $K_{hl}$, $K_{hb}$ and $K_e$ with various values of $P_{inj}$ for UMT 1, GMT 1 and LMT 1 rocks, as shown in Figs. 5(a)-5(c). $K_{hl}$, $K_{hb}$ and $K_e$ are calculated by Eqs. (8), (10) and (12), respectively. Fig. 5(a) show that permeability profiles of UMT 1 can be generally divided into three steps as $P_{inj}$ increases from 0.1 to 600 MPa:

**Step 1**: When $P_{inj} < 1$ MPa, water can only flow through hydrophilic pores and $K_{hb} = 0$. In this case, 1 MPa corresponds to the capillary pressure of maximum hydrophobic pores in UMT 1. $K_e$ represents the permeability of water in hydrophilic pores and is equal to $K_{hl}$.

**Step 2**: When $P_{inj} > 1$ MPa, water starts filling hydrophobic pores and $S_w$ of UMT1 increases. Therefore, both $K_{hb}$ and $K_e$ increase with the increasing of $P_{inj}$. However, $K_{hl}$ remains the same as $S_w$ in hydrophilic pores does not change. In addition, the shape of $K_e$ profile in this step is correlated to the contact angle in hydrophobic pores ( $\theta_{hb}$) and hydrophobic pore size distribution (PSD$_{hb}$). We will discuss the effect of $\theta_{hb}$ and PSDhb on $K_e$ in following sections.

**Step 3**: When $P_{inj} > 10$ MPa, the minimum hydrophobic pores in UMT 1 are filled by water and 100% water saturation is achieved. Further increase of $P_{inj}$ cannot make any change to $K_{hb}$ and $K_e$ and permeability profiles of $K_{hb}$ and $K_e$ reach the plateau.

Similar permeability profiles can also be observed for GMT 1 and LMT 1 rocks, as shown in Figs. 5(b) and 5(c). In addition, compared with UMT 1 and GMT 1, LMT 1 have significantly higher $K_{hb}$ than $K_{hl}$, which is in agreement with the fact that hydrophobic pores are mainly within organic matter and LMT rocks generally have higher TOC than UMT and GMT rocks. From this 3-step profile, we can obtain the value of $K_{hl}$ and $K_{hb}$ from steps 1 and 3, respectively. In addition, the $K_e$ profile in step 2 is correlated to PSD$_{hb}$.

As discussed above, $P_{inj}$ change $K_e$ by affecting $S_w$. For a more careful analysis, we derive the correlation between $P_{inj}$ and $S_w$ for the dual-wet rock. On the basis of fractal theory, $S_w$ can be calculated by:

$$S_w = \frac{V_{hlc} + V_{hbc}}{V_{hl} + V_{hb}} = \frac{\int_{\lambda_{\min\_hl}}^{\lambda_{\max\_hl}} \lambda^2 \tau_{hl} n(\lambda)\,\mathrm{d}\lambda + \int_{\lambda_{\min c\_hb}}^{\lambda_{max\_hb}} \lambda^2 \tau_{hb} n(\lambda)\,\mathrm{d}\lambda}{\int_{\lambda_{\min\_hl}}^{\lambda_{\max\_hl}} \lambda^2 \tau_{hl} n(\lambda)\,\mathrm{d}\lambda + \int_{\lambda_{\min\_hb}}^{\lambda_{\max\_hb}} \lambda^2 \tau_{hb} n(\lambda)\,\mathrm{d}\lambda} \quad (22)$$

where $V_{hlc}$ and $V_{hbc}$ are volumes of water inside hydrophilic and hydrophobic pores at a certain value of $P_{inj}$, respectively. Since we assume all the hydrophilic pores can imbibe water

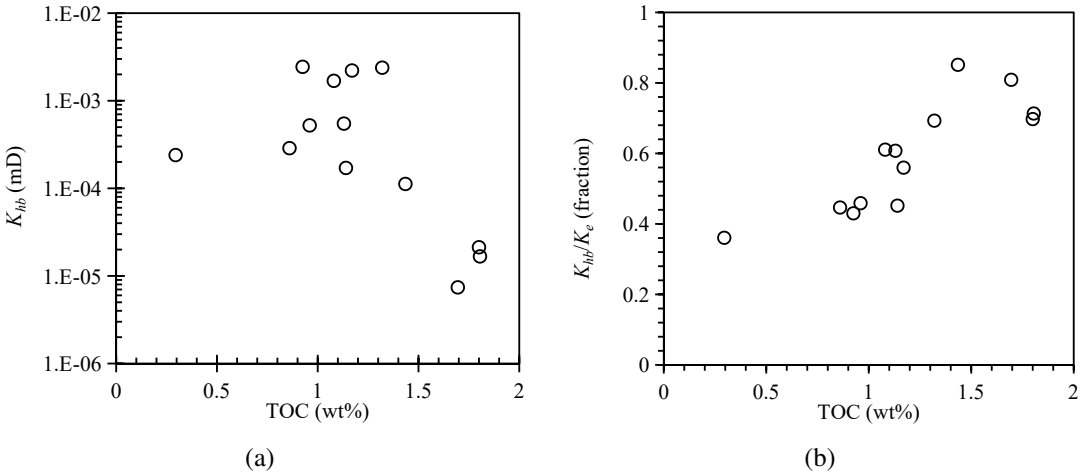


**Fig. 4**. Comparison of (a) $K_{hb}$ and (b) $K_{hb}/K_e$ vs. TOC.

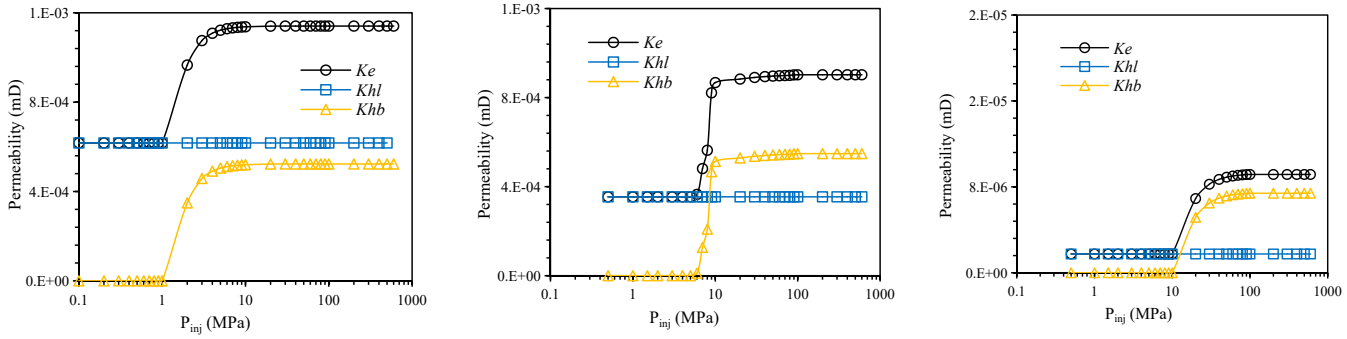


**Fig. 5**. Comparison of $K_e$, $K_{hl}$ and $K_{hb}$ versus $P_{inj}$ for (a) UMT 1, (b) GMT 1 and (c) LMT 1 rocks.

spontaneously and water saturated 100% of hydrophilic pores without any air entrapment, $V_{hlc}$ is equal to $V_{hl}$. By inserting Eqs. (3) and (7) into Eq. (22), Eq. (22) can be simplified as:

$$S_w = \frac{\phi_{hl} + f \times \phi_{hb}}{\phi_{hl} + \phi_{hb}} \tag{23}$$

where $f$ can be calculated by:

$$f = \frac{\lambda_{\max\_hb}^{2-D_{hb}} - \left(\frac{4\delta|\cos\theta_{hb}|}{P_{inj}}\right)^{2-D_{hb}}}{\lambda_{\max\_hb}^{2-D_{hb}} - \lambda_{\min\_hb}^{2-D_{hb}}} \tag{24}$$

Eq. (23) shows the correlation between $P_{inj}$ and $S_w$. As $P_{inj}$ increases, $f$ increases from 0 to 1, and $S_w$ increases from $\phi_{hl}/(\phi_{hl}+\phi_{hb})$ to 1. For a given value of $P_{inj}$, we can calculate $K_e$ by Eq. (12) and $S_w$ by Eq. (23). Figs. 6(a)-6(c) plot $K_e$ against $S_w$ for the UMT, GMT and LMT rocks. None of the curves start at $S_w$ = 0 because we assume water can spontaneously imbibe and saturate 100% of the hydrophilic pores once the rock is in contact with water. The curves start at $S_w = \phi_{hl}/(\phi_{hl}+\phi_{hb})$, which can be considered as the volumetric fraction of hydrophilic pores in the dual-wet system. As shown in Figs. 6(a)-6(c), $K_e$ is positively correlated to $S_w$. This positive correlation between $K_e$ and $S_w$ indicates that $P_{inj}$ indirectly affects $K_e$ by controlling $S_w$ of the rock. It is worth noting that, $K_e$ is conceptually different from relative permeability. In this model, we assume single phase (water) flow through capillaries, and interactions between air and water are not considered.

## 6.2 Effect of wettability

The rock wettability is generally determined either by contact angle measurement on surface of rock chips or by imbibition tests on reservoir rocks (Peters, 2012b). In this section, we firstly exam the effect of hydrophobicity of hydrophobic pores on $K_e$ by changing $\theta_{hl}$. Then, we investigate the effect of MWI on $K_e$, $K_{hl}$ and $K_{hb}$. Here, UMT 1 rock is used for the sensitivity analysis and all the parameters used in Eqs. (8), (10) and (12) are listed in Table 3.

As discussed before, the pores within or coated by organic matter tend to be hydrophobic and $\theta_{hb}$ of such pores is controlled by the thermal maturity of the organic matter (Yassin et al., 2017). In Section 5, $\theta_{hb}$ = 125° is adopted provided that the thermal maturity is generally high for the Montney rocks. Here, we change $\theta_{hb}$ from 100° to 180° and calculate $K_e$ by Eq. (12) with the parameters listed in Table 3. Fig. 7 shows the calculated $K_e$ versus $P_{inj}$. When $P_{inj}$ is around 0.1 MPa, $K_e$ is equal to $K_{HL}$ and remains the same

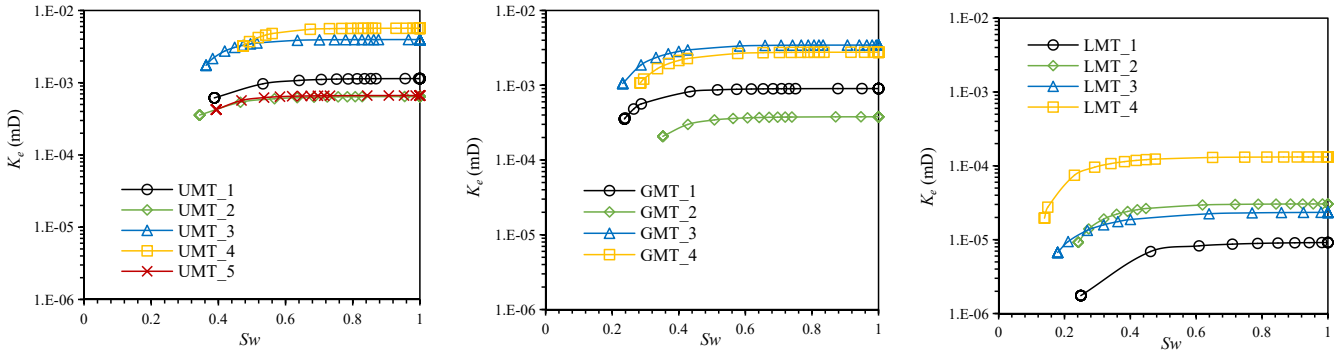


**Fig. 6**. $K_e$ versus $S_w$ for (a) UMT, (b) GMT and (c) LMT rocks.

**Table 3**. The values of parameters used in Eqs. (8), (10) and (12) for UMT 1.

| Parameters | Values | Parameters | Values |
|---|---|---|---|
| $A_f$ (cm$^2$) | 10.75 | $\lambda_{\max\_hl}$ (nm) | 131.0 |
| $\lambda_{\min\_hb}$ (nm) | 131.0 | $\lambda_{\min\_hl}$ (nm) | 12.5 |
| $\lambda_{\min\_hb}$ (nm) | 5.34 | $\phi_{hl}$ (fraction) | 0.019 |
| $\phi_{hb}$ (fraction) | 0.030 | $\tau_{hl}$ | 2.19 |
| $\tau_{hb}$ | 2.63 | $D_{hl}$ | 1.52 |
| $D_{hb}$ | 1.57 | | |

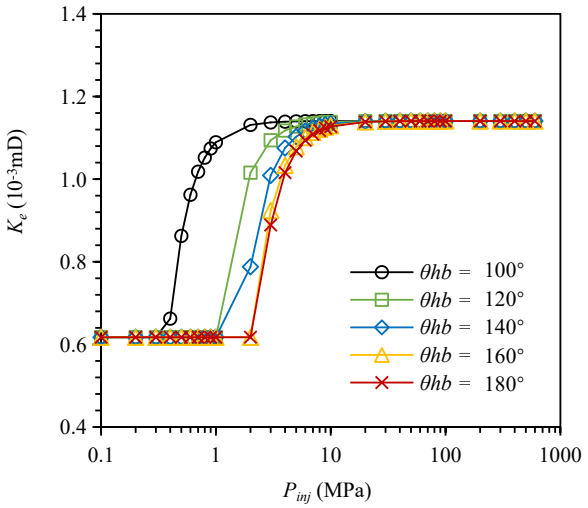


**Fig. 7**. $K_e$ versus $P_{inj}$ for different values of $\theta_{hb}$.

regardless of $\theta_{hb}$. At this point, water can just flow through hydrophilic pores and no effect of $\theta_{hb}$ can be observed. As $P_{inj}$ increases, $K_e$ starts increasing due to the water filling in hydrophobic pores and increase of $S_w$. One can observe that the rock with lower $\theta_{hb}$ needs lower $P_{inj}$ to trigger the increase of $K_e$ compared to the rock with higher $\theta_{hb}$. On the basis of Eq. (7), higher value of $\theta_{hb}$ results in higher capillary pressure of hydrophobic pores, which in turn, requires higher $P_{inj}$ to drain the air. With further increase of $P_{inj}$, $K_e$ reaches the equilibrium and 100% water saturation is achieved. The curves with higher $\theta_{hb}$ also needs higher $P_{inj}$ to reach $S_w$ = 100%. Moreover, the equilibrium value of $K_e$ remains the same for different $\theta_{hb}$. Absolute permeability depends on pore size distribution rather than wettability.

Besides contact angle, Amott wettability index has been widely used for wettability evaluation by conducting both spontaneous imbibition and forced displacement tests on reservoir rocks using oil and water (Bobek et al., 1958; Peters, 2012a). Here, MWI can be obtained by:

$$\mathrm{MWI} = \frac{\phi_{hl} - \phi_{hb}}{\phi_{hl} + \phi_{hb}} \tag{25}$$

MWI is a dimensionless number that ranges from -1 to +1. If all the pores of a rock are hydrophobic, $\phi_{hl}$ = 0 and MWI is equal to -1. Similarly, if all the pores of a rock are hydrophilic, $\phi_{hb}$ = 0 and MWI is equal to +1. For a rock that 50% of PV is hydrophilic and 50% of PV is hydrophobic, MWI is equal to 0. Therefore, as MWI increases, the water-wetness of the dual-wet rock increases.

Fig. 8(a) shows $K_e$, $K_{hl}$ and $K_{hb}$ versus MWI by using Eqs. (8), (10) and (12), respectively. Parameters listed in Table 3 are used except $\phi_{hl}$ and $\phi_{hb}$. MWI changes from -1 to +1 by changing $\phi_{hl}$ and $\phi_{hb}$ while the $\phi_{hl}$+$\phi_{hb}$ is set to be a constant value of 0.049. $P_{inj}$ is set to be 200 MPa to assure $S_w$ = 100 %. $\theta_{hb}$ = 125° is adopted. As shown in Fig. 8(a), when MWI is close to -1, $K_{hb}$ is around 0.001 mD while $K_{hl}$ approaches to 0. This is the case for a strongly oil-wet rock. As MWI increases from -1 to +1, $K_{hl}$ increases and $K_{hb}$ decreases. When MWI approaches +1, the rock can be considered to be strongly water-wet and $K_{hl}$ increases to 0.002 mD while $K_{hb}$ approaches to 0. In addition, $K_e$ increases as MWI changes from -1 to +1, as shown in Fig. 8(a). In other words, $K_{hl}$ at $\phi_{hl}$ of 0.049 is higher than $K_{hb}$ at $\phi_{hb}$ of 0.049. The reason can be explained by the different values of $D_{\min}$, $\tau$ and $D$ between hydrophilic and hydrophobic pores. As listed in Table 3, $\lambda_{\min\_hl} > \lambda_{\min\_hb}$ and $\tau_{hl} < \tau_{hb}$. Compared with hydrophilic pores, hydrophobic pores are generally smaller and more tortuous, which leads to $K_{hb} < K_{hl}$. Moreover, the lower value of $D_{hl}$ compared with that of $D_{hb}$ also contributes to $K_{hb} < K_{hl}$. The effect of D on

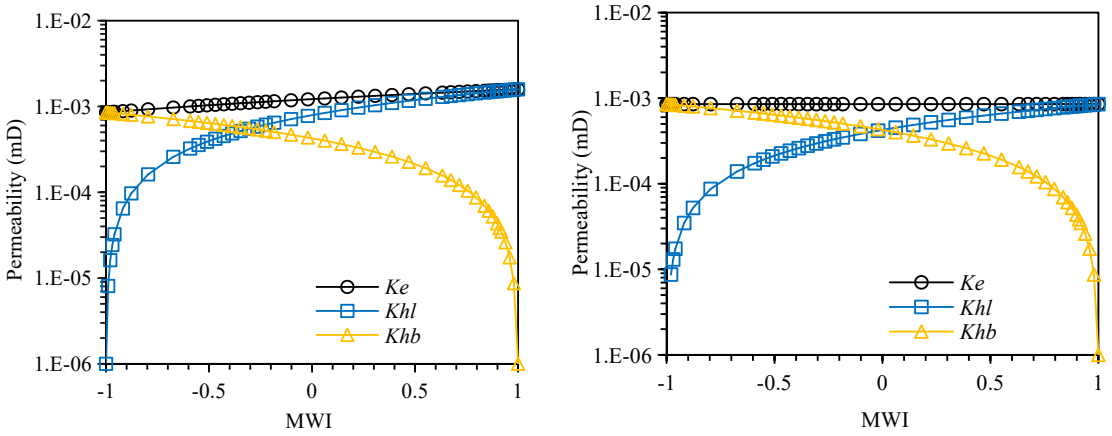


**Fig. 8**. Comparison of $K_e$ , $K_{hl}$ and $K_{hb}$ versus MWI by (a) using the parameters listed in Table 3 and (b) assuming $\lambda_{\min\_hl} = \lambda_{\min\_hb}$, $\tau_{hl} = \tau_{hb}$ and $D_{hl} = D_{hb}$.

permeability will be discussed in the following section. Here, we assume $\lambda_{\min\_hl} = \lambda_{\min\_hb}$, $\tau_{hl} = \tau_{hb}$, $D_{hl} = D_{hb}$ and plot $K_e$, $K_{hl}$ and $K_{hb}$ versus MWI, as shown in Fig. 8(b). $K_{hl}$ is positively correlated to MWI and $K_{hb}$ is negatively correlated to MWI. $K_e$ remains the same regardless of changes of MWI.

### 6.3 Effect of $PSD_{hb}$

The effect of $PSD_{hb}$ on $K_e$ is evaluated by changing $D_{hb}$ and the ratio of $\lambda_{\max\_hb}/\lambda_{\min\_hb}$. The results (as detailed in Appendix B) indicate that $K_e$ decreases as $D_{hb}$ increases. Higher value of $D_{hb}$ has larger fraction of small pores and smaller fraction of large pores. Keeping $\lambda_{\max\_hb}$ the same, $K_e$ decreases as $\lambda_{\max\_hb}/\lambda_{\min\_hb}$ increases.

## 7. Model limitations

The limitations of the proposed model have been discussed as follows:

1) The proposed model idealizes the pore network of the rock as a bundle of elongated pores with no interconnection. In this idealized pore network, all the pores are exposed to water at one end of the rock and are continuously extended to the other end of the rock. However, the water flow in the natural porous media can be more complicated if dead-end pores exist (Benavente et al., 2002; Peters, 2012a). $\phi_{hl}$ and $\phi_{hb}$ in Eq. (12) are obtained from equilibrated imbibed volume of oil and water in imbibition test. In other words, we assume all the pores that are detected by imbibition can contribute to $K_e$. In natural porous media, it is likely that the imbibed water in dead-end pores cannot contribute to the water flow even external pressure difference is applied. By ignoring the existence of dead-end pores, Eq. (12) may overestimate $K_e$.
2) We assumed that the PSD of the rock does not change during the course of water flow. The clay content in the selected Montney rocks are higher than 10 wt% (Lan et al., 2015). Clay minerals can adsorb water and expand, which could induces micro-fractures within the rock (Ghanbari and Dehghanpour, 2015). The clay expansion together with possible induced micro-fracture may considerably change the PSD. $K_e$ can be affected by the alteration of PSD, which is not considered in this model.
3) $\phi_{hl}$ and $\phi_{hb}$ in Eq. (12) are obtained from spontaneous imbibition data. Previous work (Lan et al., 2015) shows that the pore volume that detected by imbibition tests are generally smaller than the sample pore volume, estimated by helium porosimetry. As high porosity leads to high $K_e$, $K_e$ might be underestimated by obtaining $\phi_{hl}$ and $\phi_{hb}$ from available imbibition data. Furthermore, the imbibition data fails to provide effective estimation of $K_e$ if high fraction of pore volume is not detected in imbibition tests. During imbibition, snap-off mechanism can lead to air trapping.
4) As we discussed before, $\lambda_{\max\_hl}$ and $\lambda_{\max\_hb}$ in Eq. (12) are obtained from available MICP data. Mercury intrusion is a drainage process and the MICP data gives the maximum pore-throat diameter. Thus, $\lambda_{\max\_hl}$ and $\lambda_{\max\_hb}$ might be underestimated by using MICP data. This limitation can be overcome if maximum pore-body diameter can be used in Eq. (12) by assuming a reasonable aspect ratio.

## 8. Conclusions

In this paper, we proposed a fractal model for effective permeability of the rock with dual-wettability behavior. The effective permeability of $K_{hl}$ and $K_{hb}$ can also be calculated by the proposed model. The previously-proposed imbibition transient analysis technique (Shi et al., 2019) was used for determining $PSD_{hl}$ and $PSD_{hb}$ by analyzing imbibition data. The determined $PSD_{hl}$ and $PSD_{hb}$ were then used in the proposed model to calculate $K_e$, $K_{hl}$ and $K_{hb}$. Therefore, together with the imbibition transient analysis technique, the proposed model is able to estimate $K_e$, $K_{hl}$ and $K_{hb}$ of the

dual-wet rocks by using imbibition data. The $K_e$ and $K_{hb}$ were found to be dependent on injection pressure.

The proposed model is applied to calculate $K_e$ , $K_{hl}$ and $K_{hb}$ of 13 dual-wet rocks. Positive correlations have been observed for $K_e$ versus effective porosity, $K_{hl}$ versus hydrophilic porosity and $K_{hb}$ versus hydrophobic porosity. The positive correlation between the ratio of $K_{hb}/K_e$ and total organic carbon content indicates that the hydrophobic pores are primarily within organic matter for the studied rocks, which agrees with the results of scanning electron microscopy. The effect of $P_{inj}$, wettability and $PSD_{hb}$ on permeability was studied. $P_{inj}$ has no effect on $K_{hl}$ but can indirectly affect $K_e$ and $K_{hb}$ by controlling water saturation in hydrophobic pores. Higher volumetric fraction of hydrophobic pores results in higher $K_{hb}$ and lower $K_{hl}$. Keeping $\phi_{hl}$ and $\phi_{hb}$ constant, $K_e$ and $K_{hb}$ decreases as the volumetric fraction of small hydrophobic pores increases.

## Acknowledgements

We would like to thank Dr. Mahmood Reza Yassin for his kind contributions in this study. This work is supported by Open Fund of Shaanxi Key Laboratory of Advanced Stimulation Technology for Oil & Gas Reservoirs

## Supplementary file

https://doi.org/10.46690/ager.2023.05.04

## Conflict of interest

The authors declare no competing interest.



## References

Bear, J. Dynamics of Fluids in Porous Media. Princeton, USA, American Elsevier Publishing Co, 2013.

Benavente, D., Lock, P., Ángeles G., et al. Predicting the capillary imbibition of porous rocks from microstructure. Transport in Porous Media, 2002, 49(1): 59-76.

Bobek, J., Mattax, C., Denekas, M. Reservoir rock wettability-its significance and evaluation. Paper SPE 895 Presented at 32nd Annual Fall Meeting of Society of Petroleum Engineers in Dallas, Tex, 6-9 October, 1957.

Cai, J. A fractal approach to low velocity non-Darcy flow in a low permeability porous medium. Chinese Physics B, 2014, 23(4): 044701.

Cai, J., Hu, X., Standnes, D., et al. An analytical model for spontaneous imbibition in fractal porous media including gravity. Colloids and Surfaces A: Physicochemical and Engineering Aspects, 2012, 414(4): 228-233.

Carman, P. Fluid flow through granular beds. Chemical Engineering Research and Design, 1997, 75: S32-S48.

Chen, X., Yao, G. An improved model for permeability estimation in low permeable porous media based on fractal geometry and modified Hagen-Poiseuille flow. Fuel, 2017, 210: 748-757.

Davies, G. R. The Triassic of the western canada sedimentary basin: Tectonic and stratigraphic framework, paleogeography, paleoclimate and biota. Bulletin of Canadian Petroleum Geology, 1997, 45(4): 434-460.

Dullien, F. A. New network permeability model of porous media. AIChE Journal, 1975, 21(2): 299-307.

Dullien, F. A. Porous Media: Fluid Transport and Pore Structure. San Diego, New York, Academic press, 2012.

Egbobawaye, E. I. Petroleum source-rock evaluation and hydrocarbon potential in Montney Formation unconventional reservoir, northeastern British Columbia, Canada. Natural Resources, 2017, 8(11): 716-756.

Gao, L., Yang, Z., Shi, Y. Experimental study on spontaneous imbibition chatacteristics of tight rocks. Advances in Geo-Energy Research, 2018, 2(3): 292-304.

Geng, L., Li, G., Zitha, P., et al. A fractal permeability model for shale gas flow through heterogeneous matrix systems. Journal of Natural Gas Science and Engineering, 2016, 35: 593-604.

Ghanbari, E., Dehghanpour, H. Impact of rock fabric on water imbibition and salt diffusion in gas shales. International Journal of Coal Geology, 2015, 138: 55-67.

Hidajat, I., Singh, M., Cooper, J., et al. Permeability of porous media from simulated NMR response. Transport in Porous Media, 2002, 48(2): 225-247.

Jagadisan, A., Heidari, Z. Experimental quantification of the effect of thermal maturity of kerogen on its wettability. SPE Reservoir Evaluation & Engineering, 2019, 22(4): 1323-1333.

Jerauld, G., Salter, S. The effect of pore-structure on hysteresis in relative permeability and capillary pressure: Pore-level modeling. Transport in Porous Media, 1990, 5(2): 103-151.

Kozeny J. Uber kapillare Leitung des Wassers im Boden-Aufstieg, Versickerung und Anwendung auf die Bewasserung, Sitzungsberichte der Akademie der Wissenschaften Wien. Mathematisch Naturwissenschaftliche Abteilung, 1927, 136: 271-306.

Lan, Q., Dehghanpour, H., Wood, J., et al. Wettability of the Montney tight gas formation. SPE Reservoir Evaluation & Engineering, 2015, 18(3): 417-431.

Li, Z., Duan, Y., Fang, Q., et al. A study of relative permeability for transient two-phase flow in a low permeability fractal porous medium. Advances in Geo-Energy Research, 2018, 2(4): 369-379.

Mahdaviara, M., Rostami, A., Shahbazi, K. State-of-the-art modeling permeability of the heterogeneous carbonate oil reservoirs using robust computational approaches. Fuel, 2020, 268(1): 117389.

Mandelbrot, B. How long is the coast of Britain? Statistical self-similarity and fractional dimension. Science, 1967, 156(3775): 636-638.

Millington, R. J., Quirk, J. P. Permeability of porous solids. Transactions of the Faraday Society, 1961, 57: 1200-1207.

Nieto, J., Bercha, R., Chan, J. Shale gas petrophysics-montney and muskwa, are they barnett look-alikes? Paper SPWLA 200984918 Presented at SPWLA 50th Annual Logging Symposium in the Woodlands, Texas, 21-24 June, 2009.

Odusina, E. O., Sondergeld, C. H., Rai, C. S. NMR study of shale wettability, Canadian unconventional resources conference. Paper SPE 147371 Presented at the Canadian Unconventional Resources Conference, Calgary, Alberta, Canada, 15–17 November, 2011.

Perfect, E., Kay, B. Applications of fractals in soil and tillage research: A review. Soil and Tillage Research, 1995, 36: 1-20.

Peters, E. J. Advanced Petrophysics: Geology, Porosity, Absolute Permeability, Heterogeneity, and Geostatistics. Austin, USA, Greenleaf Book Group, 2012a.

Peters, E. J. Advanced Petrophysics: Dispersion, Interfacial Phenomena. Austin, USA, Greenleaf Book Group, 2012b.

Rezaee, R., Saeedi, A., Clennell, B. Tight gas sands permeability estimation from mercury injection capillary pressure and nuclear magnetic resonance data. Journal of Petroleum Science and Engineering, 2012, 88-89: 92-99.

Shi, Y., Yassin, M. R., Dehghanpour, H. A modified model for spontaneous imbibition of wetting phase into fractal porous media. Colloids and Surfaces A: Physicochemical and Engineering Aspects, 2018, 543: 64-75.

Shi, Y., Yassin, M. R., Yuan, L., et al. Modelling imbibition data for determining size distribution of organic and inorganic pores in unconventional rocks. International Journal of Coal Geology, 2019, 201: 26-43.

Tan, X., Liu, J., Li, X., et al. A simulation method for permeability of porous media based on multiple fractal model. International Journal of Engineering Science, 2015, 95: 76-84.

Wang, F., Liu, Z., Jiao, L., et al. A fractal permeability model coupling boundary-layer effect for tight oil reservoirs. Fractals, 2017, 25(5): 1750042.

Wang, W., Su, Y., Sheng, G., et al. A mathematical model considering complex fractures and fractal flow for pressure transient analysis of fractured horizontal wells in unconventional reservoirs. Journal of Natural Gas Science and Engineering, 2015, 23, 139-147.

Wardlaw, N. C., Taylor, R. Mercury capillary pressure curves and the intepretation of pore structure and capillary behaviour in reservoir rocks. Bulletin of Canadian Petroleum Geology, 1976, 24(2): 225-262.

Wardlaw, N. C., Yu, L. Fluid topology, pore size and aspect ratio during imbibition. Transport in Porous Media, 1988, 3: 17-34.

Wu, J., Yu, B. A fractal resistance model for flow through porous media. International Journal of Heat and Mass Transfer, 2007, 50(19): 3925-3932.

Xia, Y., Cai, J., Perfect, E., et al. Fractal dimension, lacunarity and succolarity analyses on CT images of reservoir rocks for permeability prediction. Journal of Hydrology, 2019, 579(6): 124198.

Xiao, D., Lu, S., Lu, Z., et al. Combining nuclear magnetic resonance and rate-controlled porosimetry to probe the pore-throat structure of tight sandstones. Petroleum Exploration and Development, 2016, 43(6): 1049-1059.

Xu, P., Yu, B. Developing a new form of permeability and Kozeny-Carman constant for homogeneous porous media by means of fractal geometry. Advances in Water Resources, 2008, 31(1): 74-81.

Yassin, M. R., Begum, M., Dehghanpour, H. Organic shale wettability and its relationship to other petrophysical properties: A Duvernay case study. International Journal of Coal Geology, 2017, 169: 74-91.

Yassin, M. R., Dehghanpour, H., Wood, J., et al. A theory for relative permeability of unconventional rocks with dual-wettability pore network. SPE Journal, 2016, 21(6): 1970-1980.

Yassin, M. R., Shi, Y., Dehghanpour, H. Pore size distribution of unconventional rocks with dual-wet pore network: A sequential spontaneous and forced imbibition technique. Paper URTEC 198316 presented at the SPE/AAPG/SEG Asia Pacific Unconventional Resources Technology Conference, Brisbane, Australia, 18-19 November, 2019.

Yu, B., Cai, J., Zou, M. On the physical properties of apparent two-phase fractal porous media. Vadose Zone Journal, 2009, 8(1): 177-186.

Yu, B., Cheng, P. A fractal permeability model for bi-dispersed porous media. International journal of Heat and Mass Transfer, 2002, 45(14): 2983-2993.

Zhang, T., Li, X., Shi, J., et al. An apparent liquid permeability model of dual-wettability nanoporous media: A case study of shale. Chemical Engineering Science, 2018, 187: 280-291.

Zhang, Y., Zeng, J., Cai, J., et al. A mathematical model for determining oil migration characteristics in low-permeability porous media based on fractal theory. Transport in Porous Media, 2019, 129(3): 633-652.

Zheng, Q., Yu, B. A fractal permeability model for gas flow through dual-porosity media. Journal of Applied Physics, 2012, 111(2): 024316.